Local distortion and octahedral tilting in BaCe$_x$Ti$_{1-x}$O$_3$ perovskite

Giorgia Confalonieri,[a]*‡ Vincenzo Buscaglia,[b] GianCarlo Capitani,[c] Giovanna Canu,[b] Nicola Rotiroti,[a] Andrea Bernasconi,[d] Alessandro Pavese[e] and Monica Dapiaggi[a]

[a]Dipartimento di Scienze della Terra, Università degli Studi di Milano, Via Botticelli 23, Milano, Italy, [b]Istituto di Chimica della Materia Condensata e di Tecnologie per l'Energia (ICMATE), Consiglio Nazionale delle Ricerche (CNR), Genova, Italy, [c]Dipartimento di Scienze dell'Ambiente e di Scienze della Terra, Università degli Studi di Milano Bicocca, Milano, Italy, [d]Dipartimento di Chimica, Università degli Studi di Pavia, Pavia, Italy, and [e]Dipartimento di Scienze della Terra, Università degli Studi di Torino, Torino, Italy. *Correspondence e-mail: giorgia.confalonieri@unito.it

Ceramics with perovskite structure and composition BaCe$_x$Ti$_{1-x}$O$_3$ (x = 0.02–0.30) show a progressive evolution with increasing x, from the long-range polar order of ferroelectric BaTiO$_3$ to the short-range polar order typical of relaxors. The ionic size mismatch between Ti^{4+} and Ce^{4+} determines strong local strains which have a significant impact on dielectric properties and phase transitions. The pair distribution function, coupled with transmission electron microscopy analysis, was applied to study the local structure. Because of the inner B-cation sizes, the superposition of rigid B—O octahedra with different volumes is not compatible with the construction of an ideal perovskite structure. In this light, local structure can be described by an original model which allows (i) different Ti—O and Ce—O distances and (ii) the typical distortions of the two end members: off-center displacement of Ti occurring in BaTiO$_3$ and octahedral tilt in BaCeO$_3$. The results show a clear difference, in terms of volumes, between oxygen octahedra with titanium and those related to cerium. In addition, the inclusion of cerium causes a tilt of its oxygen cage, as occurs in pure BaCeO$_3$, creating contra-rotations and distortions of the octahedra containing titanium. This complex arrangement entails a substantial distortion, increasing as a function of cerium amount, which strongly influences the directions of titanium displacements, their local correlation and consequently their long-range cooperative effects.

1. Introduction

Barium titanate, BaTiO$_3$ (BT), occurs in different crystallographic structures. At high temperature, it has a paraelectric cubic (C, $Pm\bar{3}m$) perovskite-type structure, which is preserved down to the Curie temperature (T_c) of 403 K. Below T_c, the structure changes to tetragonal (T, $P4mm$) and the material becomes ferroelectric. On further cooling, two other ferroelectric phases are observed: orthorhombic (O, $Amm2$) below 288 K and rhombohedral (R, $R3m$) below 193 K. All ferroelectric properties originate from specific deformations of the prototype cubic lattice caused by the off-center displacement of titanium sited in octahedral sites (Cohen, 1992). The Ti displacement gives rise to an electrical dipole at the level of the unit cell and, because of the existence of a long-range order, to a macroscopic spontaneous polarization. The structural deformations are rather small. For instance, in the tetragonal structure at room temperature, the c lattice parameter is only 1% longer than a. BaTiO$_3$ has become the most widely used functional advanced ceramic material in
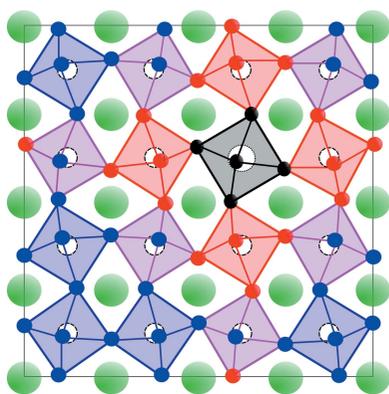
electronics. It finds wide applications in devices such as microphones, ultrasonic and underwater transducers, multi-layer ceramic capacitors, and spark generators (Yasmm *et al.*, 2011; Kishi *et al.*, 2003). In addition, it is possible to tailor its properties by chemical substitutions, meeting a greater variety of performance requirements (Acosta *et al.*, 2017; Maiti *et al.*, 2008; Jaffe *et al.*, 1971). Recently, among BT-based ferro-electric relaxors, the $BaCe_xTi_{1-x}O_3$ (BCT) solid mixture, in which Ti^{4+} is partially replaced by Ce^{4+}, has proven to be a promising lead-free material suitable in applications (Makovec *et al.*, 1996; Ianculescu *et al.*, 2016) like tunable capacitors (Curecheriu *et al.*, 2013, 2016), multilayer ceramic capacitors with high capacitance (Park & Kim, 1995) and actuators (Ang *et al.*, 2002). The incorporation of Ce^{4+} at the Ti site of $BaTiO_3$ induces remarkable changes of the phase transition temperatures and polar order, as described in detail by Canu *et al.* (2018). For $0.09 < x < 0.2$, a single R/C transition is observed, whereas the system exhibits a clear relaxor behavior and an average cubic structure for larger x values. The relaxor state is characterized by a strong frequency dispersion of the temperature, corresponding to the maximum of both real and imaginary parts of dielectric permittivity, whereas in conventional ferroelectrics T_c is independent of frequency. Relaxor behavior is associated with the presence of polar nano-regions (PNRs) embedded in a paraelectric matrix and, consequently, only short-range polar order occurs. Moreover, the polarization vectors of the single PNRs are not correlated with each other and, consequently, relaxors have no macroscopic spontaneous polarization (Shvartsman & Lupascu, 2012). Despite the much larger ionic radius of Ce^{4+} (0.87 Å, with a coordination number of 6, *i.e.* cn 6) in comparison to Ti^{4+} (0.605 Å, cn 6), the average crystal structure of the different phases appearing in the $BaCe_xTi_{1-x}O_3$ solid solution can still be described by the reference structures of undoped $BaTiO_3$. However, the larger size of the CeO_6 octahedra (14.9 Å^3; Knight, 2001) with respect to TiO_6 (10.7 Å^3; Kwei *et al.*, 1993) is likely to induce deformations of the latter, leading to a local structure (2–3 unit cells) that is expected to be quite different from the average one. In a previous paper, Canu *et al.* (2018) inferred, on the same samples, that the strain induced by the large CeO_6 octahedra is responsible for (i) the occurrence of a highly diffuse para-electric/ferroelectric transition even at low cerium concentration ($x = 0.05$) and (ii) the nearly constant T_c value measured up to $x = 0.10$. For the sake of comparison, in the homologous system $BaSn_xTi_{1-x}O_3$ (the ionic radius of Sn^{4+} is 0.69 Å, cn 6), a diffuse phase transition only occurs when $x > 0.10$ and T_c strongly decreases from 403 to 320 K ($x = 0.10$) (Lei *et al.*, 2007). Therefore, the macroscopic properties of the material are defined not only by the long-range structure but also by the short-range atomic arrangements. This work aims to provide a full local structure analysis, which is to be compared with the average one, using synchrotron radiation powder elastic scattering, the traditional Rietveld method, pair distribution function (PDF) refinements (Billinge & Thorpe, 1998; Egami & Billinge, 2012) and semi-classical modeling. Transmission electron microscopy (TEM), with

Table 1
Composition, data collection temperature and polar order as inferred from dielectric measurements of investigated samples.

DPT: ferroelectric with diffuse phase transition.

Composition	Temperature (K)	Polar order (Canu *et al.*, 2018)
$BaTi_{0.98}Ce_{0.02}O_3$ ($x = 0.02$)	150, 270, 350, 450	Ferroelectric
$BaTi_{0.95}Ce_{0.05}O_3$ ($x = 0.05$)	200, 350, 380, 420	DPT
$BaTi_{0.9}Ce_{0.1}O_3$ ($x = 0.10$)	100, 200, 300, 400	DPT
$BaTi_{0.8}Ce_{0.2}O_3$ ($x = 0.20$)	100, 200, 300, 400	Relaxor
$BaTi_{0.7}Ce_{0.3}O_3$ ($x = 0.30$)	100, 200, 300, 400	Relaxor

energy dispersive X-ray spectroscopy (EDS) microanalyses, is used to investigate the degree of homogeneity of the Ce distribution throughout the samples under study.

2. Experimental

2.1. Sample preparation

$BaCe_xTi_{1-x}O_3$ (BCT) ceramic samples with various compositions ($x = 0.02, 0.05, 0.10, 0.20$ and 0.30) corresponding to different polar behaviors were prepared according to the limit of the solid solubility of Ce^{4+} in $BaTiO_3$, which is about $x = 0.33$ (Lu *et al.*, 2012; Makovec *et al.*, 1996). High-purity $BaCO_3$ (Solvay Bario e Derivati, Massa, Italy), TiO_2 (Toho Titanium, Chigasaki, Japan, grade HT2301) and CeO_2 (Degussa, VP AdNano Ceria 50, Evonik Degussa, Hanau, Germany) nano-powders were used in the synthesis as precursors. $BaCe_xTi_{1-x}O_3$ powders were obtained by the solid state reaction

$$BaCO_3 + (1 - x)TiO_2 + xCeO_2 \rightarrow Ba(Ce_xTi_{1-x})O_3 + CO_2. \quad (1)$$
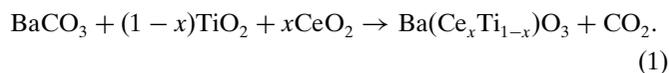
The reagents were wet-mixed for 24 h using distilled water and, after freeze-drying, the blend was calcined at 1273 K for 4 h to promote the solid-state reaction and sieved. The resulting powders were compacted into cylinders (length: 1 cm; diameter: 1 cm) by cold isostatic pressing at 1500 bar (150 MPa), and then sintered at either 1723 K ($x = 0.02$–0.10) or 1823 K ($x = 0.20$–0.30) for 4 h. The density of the final ceramic output was measured by the Archimedes method. The incorporation of Ce^{4+} at octahedral sites was proved by measuring dielectric properties and Raman active frequencies and by collecting X-ray diffraction patterns, which show the absence of the characteristic peaks attributable to secondary phases (Canu *et al.*, 2018).

2.1.1. Data collection. Powder diffraction data were collected at the high-resolution powder diffraction beamline ID22, ESRF, Grenoble, France (https://www.esrf.eu; Fitch, 2004). In Table 1, the samples and related data collection conditions are reported. Measurements were performed at different temperatures, with the purpose of getting insight into the evolution of the samples' crystal structures.

$x = 0.05$, $x = 0.10$ and $x = 0.20$ sample compositions. The beam wavelength ($\lambda = 0.294932$ Å) was set by a channel-cut Si(111) crystal monochromator. Diffracted intensity was

detected, as a function of 2θ, by a bank of nine detectors, each preceded by an Si(111) crystal analyzer. Measurements were performed at room temperature on standard Si and an empty borosilicate glass capillary. *In situ* data collections of the BCT powders, contained in borosilicate glass capillaries of 0.6 mm diameter, were carried out using an Oxford Cryosystems Cryostream cold-nitrogen-gas blower sample environment. Given that total scattering analysis requires highly reliable counting statistics, especially at high Q (momentum transfer) values (in this case experimental $Q_{max} = 30$ Å^{-1}), data collection times of 4 h were chosen.

$x = 0.02$ and $x = 0.30$ sample compositions. A wavelength of 0.154972 Å, determined using LaB$_6$ standard material, and an appropriate sample–detector distance were chosen to obtain a high Q value (experimental $Q_{max} = 29$ Å^{-1}). Diffraction intensities were recorded by a two-dimensional detector, a PerkinElmer XRD 1611CP3 flat panel. For all samples and an empty capillary, 60 images (exposure time 25 s) were collected, averaged and integrated. Later, samples were re-measured during a separate experiment using a multianalyzer detector, to collect high-resolution data, and a wavelength of 0.335014 Å. In both experiments, the samples were ground, put into borosilicate glass capillaries of 0.6 mm diameter and then measured at different temperatures, using the Oxford Cryosystems Cryostream cold-nitrogen-gas blower.

2.1.2. Rietveld refinements, PDF calculation and analysis. Diffraction patterns were analyzed with the Rietveld method using the *Maud* software (Lutterotti *et al.*, 1999). Background, r.m.s. microstrain, crystallite size, cell parameters, atomic positions (according to the space group rules) and isotropic displacement parameters were refined to fit theoretical patterns to the experimental ones. Spurious signals due to the instrumentation were accounted for by means of Si standard material, measured under the same conditions used for the samples under investigation. The r.m.s. microstrain and crystallite size were determined using the isotropic model. In the structural refinement, titanium and cerium are modeled by fractional occupancy factors and constrained to share the same position. In order to obtain PDFs, total scattering data were corrected and normalized by the use of the *PDFgetX3* software (Juhás *et al.*, 2013). PDFs were calculated in the same way for all the samples under investigation to guarantee a full comparison: $q_{max\ inst}$ was fixed at 27 and q_{max} at 26, r_{poly} (Juhás *et al.*, 2013; Confalonieri *et al.*, 2015) was 1.4, and q_{min} was 0. An empty capillary, collected at room temperature, was used for the background subtraction and bgscale (Juhás *et al.*, 2013; Confalonieri *et al.*, 2015) was fixed at 1. This procedure allows the elimination of capillary, instrument and air contributions. PDF analyses were performed with the *DiffPy-CMI* (Juhás *et al.*, 2015) and *PDFgui* software (Farrow *et al.*, 2007). Standard materials (Si and LaB$_6$) were used to set the Q_{damp} parameters (one for each experiment).

2.1.3. TEM. TEM observations at room temperature were performed at the Department of Physical Sciences, Earth and Environment of the University of Siena with a JEOL JEM 2010 operating at 200 keV and equipped with an Oxford Link energy-dispersive spectrometer for EDS microanalysis and

with an Olympus Tengra $2300 \times 2300 \times 14$ bit slow scan CCD camera for image acquisition. Two types of sample preparation were adopted:

(i) Powder sample. The sample was ground and the obtained powders were dispersed in ethanol and ultrasonicated. Then a 5 ml drop of the suspension was deposited on a carbon-coated Cu grid.

(ii) Ion-milled sample. The sample was mechanically thinned with silicon carbide paper, double polished with alumina, fixed on a Cu ring and then gently ion-milled down to electron transparency. Ion milling was carried out with a Gatan precision ion polishing system (PIPS). Finally, the sample was carbon coated to avoid electrostatic charging during TEM observations.

3. Results and discussion

3.1. Average structure

Cerium introduction in BaTiO$_3$, as above reported, generates structural changes, at different levels, as a function of Ce amount. The space groups and the lattice parameters *versus* temperature and composition are summarized in Table 2 (columns 2–4) and described in detail, along with their influence on the material dielectric properties, by Canu *et al.* (2018). In the present article we focus on short/long-range structure order of Ce-doped BaTiO$_3$. In the structural refinements, along with the cell parameters and isotropic displacement parameters for each atomic site, the B-cation position, taken by Ti and Ce with occupancy factors corresponding to their nominal fractional amounts, was refined according to the space group constraints. In particular, Ti/Ce has coordinates (xxx) in space group $R3m$, ($1/2\ 0\ z$) in $Amm2$ and ($1/2\ 1/2\ z$) in $P4mm$. No B-cation displacement is allowed in the cubic symmetry (B cation at special position $m\bar{3}m$).

The titanium displacement for pure BaTiO$_3$ (Kwei *et al.*, 1993) and Ti/Ce displacement in BaCe$_x$Ti$_{1-x}$O$_3$ calculated with respect to the center of the corresponding unit cells are shown in Fig. 1. For every explored temperature, the B-cation displacement decreases with increasing Ce content, and it completely disappears in the cubic structure.
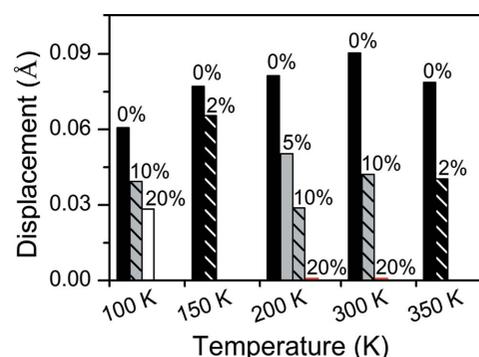

Figure 1
B-cation displacements at different temperatures for doped and pure barium titanate. Displacements equal to zero, as the crystal system is cubic, are reported in red.

Table 2
Cell and angle parameters related to the average, obtained by Rietveld analysis (Canu *et al.*, 2018), and local structure, from PDF refinements between 1 and 20 Å.

The data sets indicated by an asterisk (*) are slightly biphasic. Local structural results for $x = 0.02$ were obtained by refining the simple model; for the other samples the tilt model was used.

Sample	Average space group	Average cell parameter (Å)	Average cell angle (°)	Local space group	Local cell parameter (Å)	Local cell angle (°)
$x = 0.02$ 150 K	$R3m$	4.01366 (5)	89.8727 (3)	$R3m$	4.0094 (6)	89.687 (4)
$x = 0.02$ 270 K*	$Amm2$	4.0003 (7)		$R3m$	4.0120 (9)	89.638 (7)
		5.6837 (1)				
		5.6966 (1)				
$x = 0.02$ 350 K	$P4mm$	4.01025 (2)		$R3m$	4.0133 (9)	89.573 (6)
		4.03381 (3)				
$x = 0.02$ 450 K	$Pm\bar{3}m$	4.02068 (1)		$R3m$	4.0175 (9)	89.561 (7)
$x = 0.05$ 200 K	$R3m$	4.02849 (1)	89.8858 (2)	$R3m$	4.0299 (6)	89.602 (1)
$x = 0.05$ 300 K*	$Amm2$	4.0246 (1)		$R3m$	4.0322 (7)	89.691 (5)
		5.7013 (1)				
		5.7085 (1)				
$x = 0.05$ 350 K*	$P4mm$	4.02827 (1)		$R3m$	4.0333 (8)	89.607 (4)
		4.03952 (2)				
$x = 0.05$ 380 K	$Pm\bar{3}m$	4.03253 (2)		$R3m$	4.0340 (9)	89.608 (5)
$x = 0.05$ 420 K	$Pm\bar{3}m$	4.034492 (7)		$R3m$	4.0355 (1)	89.583 (6)
$x = 0.10$ 100 K	$R3m$	4.04856 (1)	89.8740 (2)	$R3m$	4.0494 (5)	89.587 (2)
$x = 0.10$ 200 K	$R3m$	4.05107 (1)	89.8896 (2)	$R3m$	4.0522 (6)	89.543 (2)
$x = 0.10$ 300 K	$R3m$	4.05397 (1)	89.980 (1)	$R3m$	4.0551 (8)	89.502 (3)
$x = 0.10$ 400 K	$Pm\bar{3}m$	4.05672 (1)		$R3m$	4.0580 (1)	89.450 (4)
$x = 0.20$ 100 K	$R3m$	4.09255 (1)	89.957 (2)	$R3m$	4.0945 (7)	89.450 (2)
$x = 0.20$ 200 K	$Pm\bar{3}m$	4.0951 (1)		$R3m$	4.0970 (8)	89.413 (3)
$x = 0.20$ 300 K	$Pm\bar{3}m$	4.09814 (1)		$R3m$	4.1002 (1)	89.392 (3)
$x = 0.20$ 400 K	$Pm\bar{3}m$	4.10164 (1)		$R3m$	4.1037 (1)	89.369 (4)
$x = 0.30$ 100 K	$Pm\bar{3}m$	4.13523 (2)		$R3m$	4.1317 (9)	89.403 (3)
$x = 0.30$ 200 K	$Pm\bar{3}m$	4.13774 (2)		$R3m$	4.1336 (1)	89.393 (3)
$x = 0.30$ 300 K	$Pm\bar{3}m$	4.14094 (2)		$R3m$	4.1368 (1)	89.375 (4)
$x = 0.30$ 400 K	$Pm\bar{3}m$	4.14465 (2)		$R3m$	4.1410 (2)	89.331 (4)

It is worth noting the occurrence of a significant reduction of the *B*-site displacement in all the Ce-bearing compositions, with respect to the pure BaTiO$_3$ phase. However, a direct comparison is to be made with due care, as in traditional crystallography the species giving a solid mixture are placed on the same crystallographic site, with fractional occupancies. Here, the cerium cations are expected not to shift off the
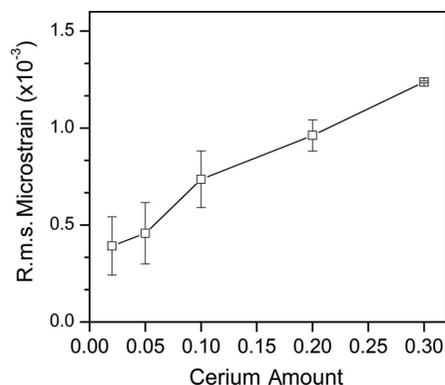

Figure 2
Comparison of r.m.s. microstrain as a function of cerium amount. For each sample, the mean r.m.s. microstrain, averaged over the different temperatures, and its estimated standard deviations are reported.

center of the octahedron, owing to their large ionic radii, whereas titanium is likely to be affected by a displacement. However, the separate treatment of the substituents is difficult to achieve in conventional crystallographic refinements, and one has to rely on super-cell methods (like, for instance, reverse Monte Carlo methods) and/or on techniques based on total scattering data.

The average structure analysis with the Rietveld method indicates that the introduction of the large Ce ion in the BaTiO$_3$ lattice generates a non-negligible strain, observable as r.m.s. microstrain. Fig. 2 shows the average r.m.s. microstrain (a.r.m.s.), which monotonically increases as a function of the Ce content. For each composition, a.r.m.s. was calculated by averaging the r.m.s. values at different temperatures (excluding biphasic samples); the error bars represent the related standard deviations.

The incorporation of Ce^{4+} in the perovskite-type lattice also affects the ferroelectric order, thus determining a misorientation of the dipoles and a change of their magnitude. Raman spectroscopy (Canu *et al.*, 2018) reveals a degree of disorder related to the cerium introduction. The Raman modes appear broadened in comparison to those of undoped BaTiO$_3$ and phase transitions occur over a certain temperature range rather than at a given temperature. All this points to the need to undertake a local structure characterization and modeling, by means of the PDF analysis.

3.2. Local structure

3.2.1. PDF features. Fig. 3 shows the PDFs at the lowest available temperature for each studied composition ($x = 0.02$–0.30), compared with the PDF of the reference rhombohedral structure of BaTiO$_3$ (the top black profile in the figure), in the ranges from 1 to 8 Å and from 10 to 18 Å. A progressive broadening of the peaks, as a function of the increasing Ce content (from bottom to top), is readily observed. Peak broadening in a PDF can be attributed either to a dynamic disorder (mainly thermal vibrations, more severe at high temperature) or to a static disorder (for instance, intra- and inter-polyhedron distortion). We are inclined to attribute the peak broadening to static disorder, as dynamic disorder is supposed to be unlikely at about 100 K. A further effect due to cerium introduction can be seen in the first peak of the PDFs (at $r \simeq 2$ Å), which is associated with the nearest neighbors (*i.e.* with the Ce—O and Ti—O bond lengths in the octahedron). Such a peak, which must occur though with modest intensity (as shown in the black theoretical rhombohedral

$BaTiO_3$ PDF at the top of the figure, labelled B-O), is often severely obscured by the background noise, *i.e.* by the termination ripples, which affect particularly the short-*r*-value region. This effect is enhanced by the likely broad distribution of $B-O$ distances, due to the different type and strength of the distortion of the TiO_6 and CeO_6 octahedra, like in the homologous $BaZr_xTi_{1-x}O_3$ (BZT) system (Laulhe *et al.*, 2009). All this makes it difficult to formulate reasonable hypotheses about the distribution of the distance between nearest cation–oxygen pairs ($Ti-O$ and $Ce-O$).

3.2.2. Simple model. BCT exhibits local rhombohedral symmetry regardless of composition and temperature, as reported by Canu *et al.* (2018). According to their Rietveld refinements, some data sets were composed of two phases (O + R for *x* = 0.02 at 270 K, O + R for *x* = 0.05 at 300 K and T + O at 350 K). However, considering the small amount of the secondary phases (approximately estimated as 2–3 wt%), all the samples at local level were considered as monophasic and locally refined using a single structure. PDF fits, reported in Fig. 3 with red lines, were performed over the range 1–20 Å using the rhombohedral structure found in the literature (Kwei *et al.*, 1993) and a $2 \times 2 \times 2$ supercell, to explore more realistic models for the local disorder involving in particular Ti and Ce. As a starting point, Ti and Ce were constrained at the same position and with the fractional occupancy factors from Rietveld refinements. A satisfactory fitting is obtained over the range 10–20 Å, whereas a worsening of agreement is observed at shorter distances. In particular, the calculated profiles associated with peaks at ~3.5 Å (Ba−*B* distances) and ~4 Å (second *B*−O distances) match the experiments poorly, in terms of shape, height and position. These results indicate the presence of a substantial local disorder. There are many possible origins of such a disorder, and they need to be explored separately and, eventually, combined together, for a better understanding. In order to provide a specific and realistic description of the local disorder, the development of a possible structural model was divided into two steps. In the first step, the *B*-cation distribution is explored (§3.2.3), and in the second, oxygen positions and related disorder are explored (§3.2.4).

3.2.3. *B*-cation disorder. The distribution of cations (whether random or clustered) within a solid solution has a non-negligible influence on the diffuse scattering and therefore on the related PDF in the local and medium-range regions. Since it is difficult to distinguish the diffuse scattering related to cation distribution from the contributions of other sources, such as the presence of defects or non-crystalline phases, TEM investigations were undertaken. For this task, we selected the sample with *x* = 0.20, *i.e.* a sample with a Ce content large enough to allow, in principle, an easy detection of any presence of domain structure due to cation segregation. Low-magnification bright-field (BF) images do not show amorphous domains or any other kind of domain structure, but rather perfect polygonal texture with angles between grains close to 120°, which is usually considered a thermodynamic equilibrium texture (Fig. 4*a*). Consistently, selected area diffraction (SAD) patterns taken on single grains along principal crystallographic directions show perfect long-range order (Figs. 4*b* and 4*c*), with diffraction spots free of streaking or satellite reflections indicative of disordered intergrowths and superstructures, respectively. Moreover the high-resolution (HR) TEM images show a contrast consistent with a single-crystal ordered structure (Figs. 4*d* and 4*e*). However, this apparent perfection, which entails a homogenous distribution of cerium cations, is impaired by dislocations that can be imaged at low magnification under specific diffraction conditions (Fig. 5). The dislocation density appears large in comparison to non-metamorphic natural samples or synthetic deformed samples prepared in the same way, in spite of the fact that the sample shows a typical equilibrium texture. Dislocations may cause local distortion of lattice planes and anomalous cation coordination that can greatly contribute to the diffuse scattering.

The homogeneity of the sample was checked also by TEM-EDS, collecting spot analyses on
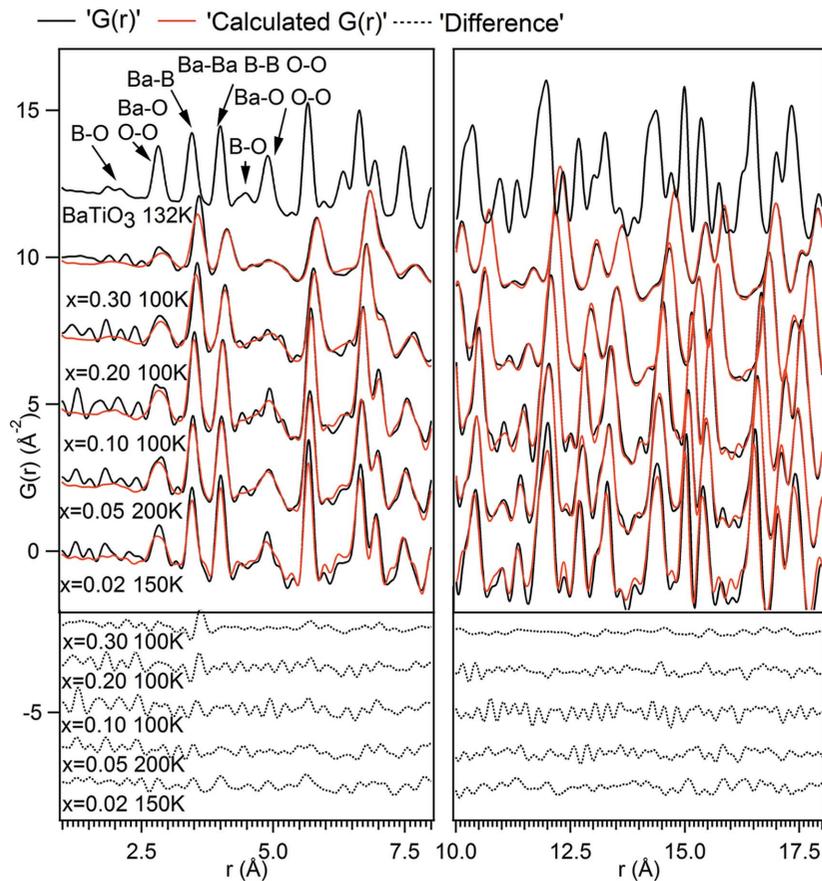

Figure 3
PDF local fits between 1 and 20 Å, obtained by refining the simple model. At the top, the theoretical PDF, obtained using the bibliographic $BaTiO_3$ rhombohedral structure (Kwei *et al.*, 1993), is reported.

randomly selected thin areas of different grains of the powdered sample (nominal spot size 25 nm). Note, however, that the Ti $K\alpha$ (~4.51 keV) and the Ba $L\alpha$ (~4.46 keV) lines are difficult to distinguish with the EDS system, whose reso-

lution is estimated to be ~60–70 eV, and Ce $L\alpha$ is practically superposed with Ba $L\beta$ (~4.83 keV). Therefore, the analyses could be severely affected by this instrumental limitation, but still internally consistent. In other words, although they show a systematic error in accuracy, they should be capable of revealing any chemical difference between the different analyzed grains. The results (Table 3) show that, while the Ce content is almost constant and consistent with the stoichiometric value, Ba and Ti exhibit variations of the order of a few wt%, with a systematic Ba excess and Ti deficiency with respect to the expected formula. The Ti deficiency is due to the systematic error mentioned above. Taking into account that the sensitivity of TEM-EDS analysis is ~1–2 wt%, we conclude that no significant anomalous distributions of Ba, Ti and Ce atoms among different grains could be unveiled by TEM-EDS. We can therefore assume that in BCT $x = 0.20$ perovskites the local disorder is not associated with any special Ce distribution or Ce—Ce interaction. This is consistent with the observations of the pair distribution functions: a Ce-rich cluster will have a larger (with respect to a random distribution) probability of a Ce—Ce nearest cation neighbor, and therefore a greater intensity of the PDF peak at about 4 Å, more noticeable with increasing cerium content.

Figure 4
BCT $x = 0.20$ perovskite. (a) BF image showing a perfect polygonal equilibrium texture with triple junctions between grains forming angles of ~120°. (b), (c) SAD patterns taken along [010] and [101], respectively, showing perfect long-range order. Note that the same patterns could be indexed as [001] and [110], respectively, because of the very similar b (5.6214 Å) and c (5.6386 Å) cell parameters of the orthorhombic cell used for indexing (Xiao *et al.*, 2008). (d), (e) HR images taken with beam incidence as in (b) and (c), respectively, with homogeneous contrast.

3.2.4. Oxygen disorder and tilt model. So far, we have some indications that the evident disorder introduced by cerium atoms in the BaTiO₃ lattice cannot be related to a particular spatial distribution of cerium ions, and that there must be some other origin of the deviation from ideal.

Oxygen atoms and their positions are explored next, as they can be the source of local disorder (Gatta *et al.*, 2013).

First, with the aim of understanding in which radius (r) region the local disorder is more pronounced, a 'carbox' approach was followed. This strategy encompasses PDF refinements in different r regions with the aim of evaluating the coherent correlation length of a disordered structure. In this case, instead, different radius ranges are refined independently in order to define in which region the crystallographic ideal structure required modifications
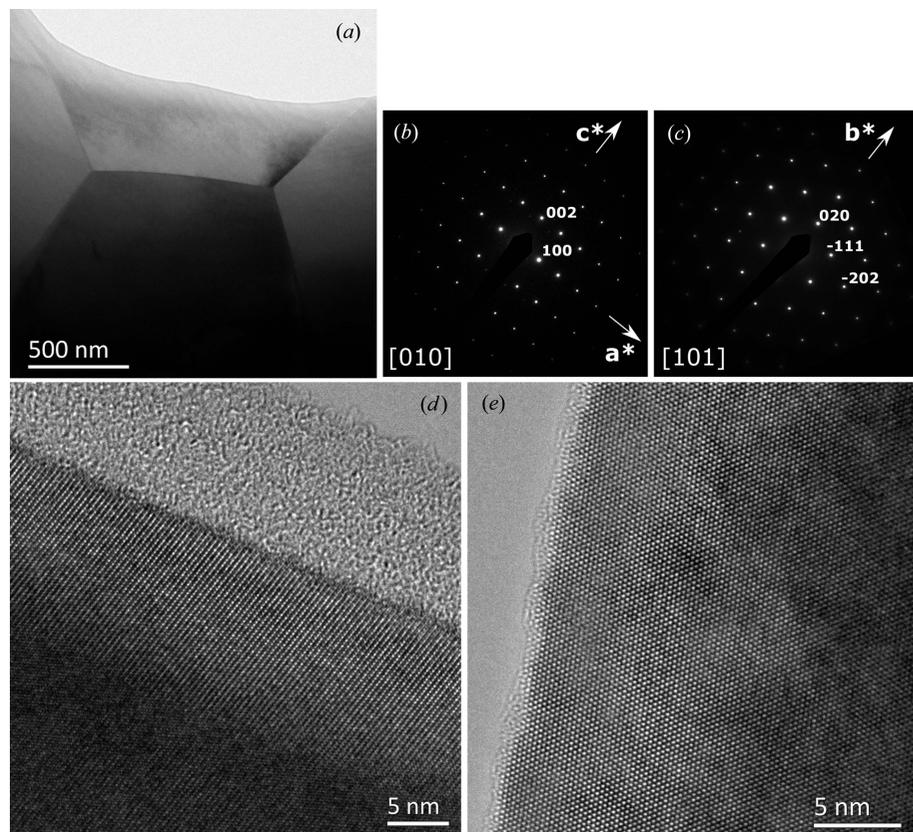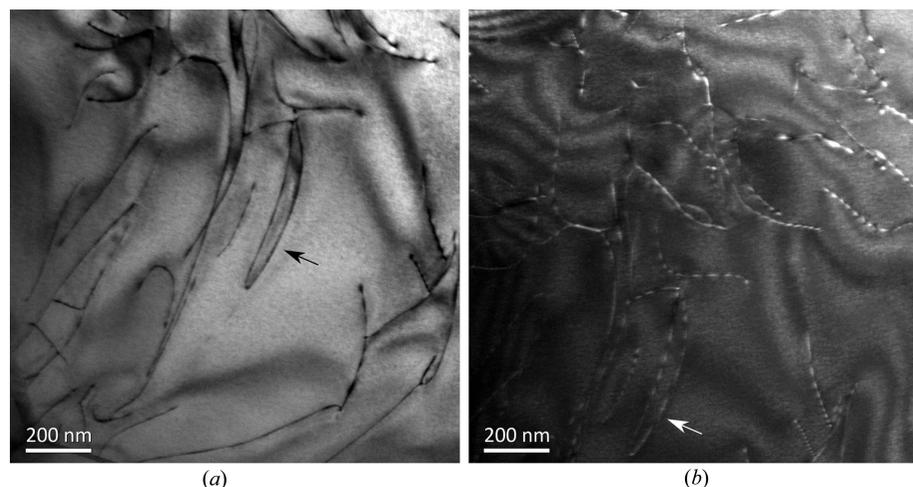

Figure 5
Bright-field (a) and dark-field (b) images of BCT $x = 0.20$ perovskite, showing a high density of dislocations (arrows in the images point to the same dislocation loop).

Table 3
TEM-EDS compositions of BCT ($x = 0.20$) perovskite given as cation wt% and recalculated assuming two cations in the formula.

Each column represents the average of several spot analyses (whose number is indicated in brackets) taken on different grains of four different areas of the sample. Numbers in brackets on the right side of the columns represent standard deviations.

wt%	1 (7)	2 (8)	3 (5)	4 (12)
Ti	14.8 (1.5)	12.3 (0.4)	11.3 (1.4)	13.8 (0.9)
Ba	72.1 (2.5)	76.3 (1.1)	76.7 (1.3)	73.6 (2.0)
Ce	13.1 (1.5)	11.4 (1.0)	12.0 (1.3)	12.6 (1.8)
Cations per formula unit				
Ti	0.67 (0.05)	0.57 (0.01)	0.53 (0.05)	0.63 (0.03)
Ba	1.13 (0.06)	1.24 (0.02)	1.27 (0.04)	1.17 (0.04)
Ce	0.20 (0.02)	0.18 (0.02)	0.20 (0.02)	0.20 (0.03)

(as larger static atomic displacements) to fit the data. Thereby, it may be possible to recognize in which region the local disorder is more severe and to try out a structure model. Three radius ranges were considered: 1–5.5, 5.5–10 and 10–14.5 Å. A rhombohedral $2 \times 2 \times 2$ supercell (in order to be able to refine cerium and titanium ions independently of one another) was chosen; as a starting point, titanium and cerium were constrained in the same site, with fractional occupancies. Two refinement strategies were selected:

(1) Strategy A: oxygen positions as (xxz) were refined, together with cell parameters.

(2) Strategy B: like A, but with the additional refinement of Ce and Ti positions (xxx), independently of one another.

In Fig. 6 the oxygen displacements obtained for all the samples at the lowest temperature are reported for the two strategies in each radius range considered. Displacements are calculated from the center of the rhombohedral cell faces. Whichever strategy one chooses, the second range (5.5–10 Å) requires larger oxygen movements to fit the data. This suggests a disorder not only related to nearest neighbors but most probably associated with the linking between different octahedra (*i.e.* within this r range). We stress that these fits have no purpose of identifying the structural model of disorder; they are used only to establish in which r range the disorder mostly manifests itself.

One possible model to explain the disorder in this medium r region could involve a tilt of the octahedra. Owing to the symmetry of the space group, this type of distortion is not allowed in pure $BaTiO_3$ (Thomas & Beitollahi, 1994), where, in fact, the properties of ferroelectric phases are related mainly to titanium displacements within the octahedra (Miura *et al.*, 2011; Müller *et al.*, 1987; Müller & Berlinger, 1986; Comès *et al.*, 1970). However, other perovskites show a certain degree of BO_6 octahedral tilting, which shortens the distance $A-O$ without losing polyhedral corner-sharing connectivity (Woodward, 1997). This happens, for instance, in $BaCeO_3$ (de Souza & Muccillo, 2010). Given that preservation of the polyhedral connection and bond length of its end members is common in solid mixtures, one can assume that Ce-bearing octahedra behave like those in pure $BaCeO_3$, with some degree of tilting. This, in turn, might induce a tilt in neigh-

boring Ti—O polyhedra, or at least some degree of internal deformation, giving rise to six non-equal Ti—O distances (Laulhe *et al.*, 2009). This is in agreement with the experimental PDFs, wherein the disorder at short r values, for any explored temperature and composition, is associated with the first $B-O$ peak, which is so broad as to be almost completely hidden by termination ripples. As already discussed, the broad peak may be due, in this case, to a distribution of slightly different Ti—O and Ce—O distances in distorted polyhedra.

In the light of these features shown by the experimental PDFs and keeping in mind that the largest differences from the ideal structure lie in the inter-octahedral region, a structural model consistent with observations requires that slightly distorted octahedra can tilt, without losing their corner-sharing connectivity. This structural model, dubbed the 'tilt model', was refined using data between 1 and 20 Å and is detailed below.

The sample with $x = 0.02$ is not included in this modeling. The low cerium amount is probably too small to induce a detectable tilting effect. However, the results for $BaTi_{0.98}Ce_{0.02}O_3$ obtained using the simple rhombohedral structure (named the 'simple model') will be presented for the sake of comparison with the other results.

The starting configuration for the tilt model is built as a rhombohedral $4 \times 4 \times 4$ supercell. The supercell is necessary here in order to avoid fractional occupancies of Ti and Ce; its size ($4 \times 4 \times 4$) allows us to consider at least three cerium atoms for each composition. For all the explored compositions, Ce cations were positioned in order to be linked only to Ti polyhedra (mimicking the right stoichiometry for the different BCTs; *e.g* in $x = 0.20$, 13 of the 64 octahedra are coordinated by cerium atoms).
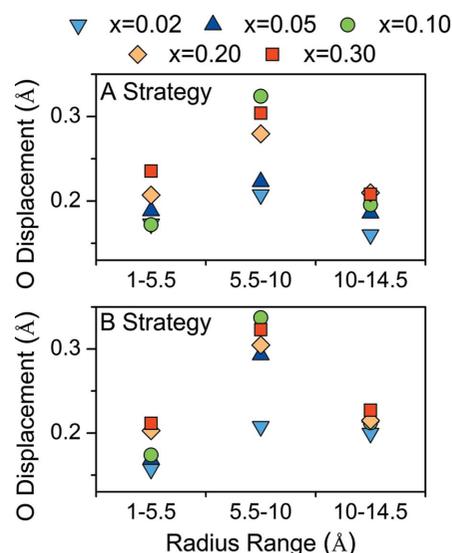

Figure 6
Oxygen displacements, calculated from the center of the rhombohedral cell face, obtained by refining PDFs using two different strategies with a carbox approach. Only results related to the lowest temperatures are presented; errors are not reported because they are not significant in the comparison of results in the three ranges.

All octahedra are set in order to rotate and contra-rotate with respect to each other. Even though space group $R3m$ does not allow all the rotations described below, some of its restraints are used in order to reduce the number of refined parameters, which, in such a large unit cell, may become unmanageable and lead to physically unsound results.

Three of the O atoms in each octahedron move, respectively, according to $(1/2 + \Delta x, 1/2 + \Delta x, 0 + \Delta z)$, $(1/2 + \Delta x, 0 + \Delta z, 1/2 + \Delta x)$ and $(0 + \Delta z, 1/2 + \Delta x, 1/2 + \Delta x)$, using the symmetry constraints of space group $R3m$. At the same time, the other three oxygen atoms within the same octahedron are constrained to move in the opposite direction, *i.e.* $(1/2 - \Delta x, 1/2 - \Delta x, 0 - \Delta z)$, $(1/2 - \Delta x, 0 - \Delta z, 1/2 - \Delta x)$ and $(0 - \Delta z, 1/2 - \Delta x, 1/2 - \Delta x)$ (Fig. 7). In Glazer's notation (Glazer, 1972), this creates an $a^- a^- a^-$ tilt type.

Furthermore, octahedra were divided into different groups (Fig. 7), depending on their distance from cerium octahedra (shown in black in the figure), and their oxygen atoms were refined differently. O atoms belonging to different groups are constrained to move by different Δx and Δz in order to induce the necessary distortion in the octahedra (differences in Ti—O bond lengths and between Ti- and Ce-bearing octahedra). Cerium ions, because of their size, were kept at fixed positions in the refinements, while the related octahedra are free to rotate and expand, but with six equal Ce—O bond lengths
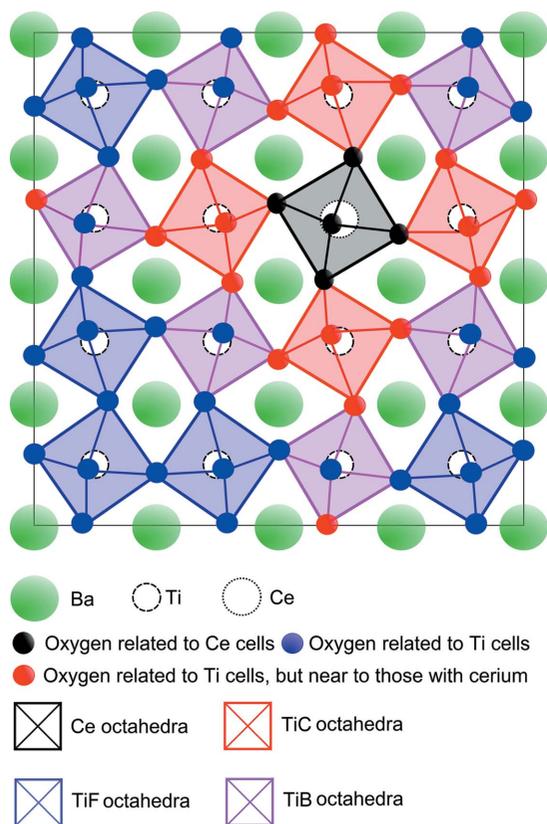
(this is obviously not true for Ti-bearing octahedra, as one can infer from above). Three classes were developed for TiO_6: octahedra close to those with cerium (called from now on TiC, the red octahedra in Fig. 7), octahedra far from those with cerium (called TiF, the blue octahedra in Fig. 7) and those in between these two extremes (called TiB, the purple octahedra in Fig. 7). Depending on cerium amount, samples could contain octahedra belonging to one, two or three of these classes. For example, only for $x = 0.05$ is it possible to find some TiF (far from cerium, at a distance of ~16 Å between the two centers). With increasing Ce content, more Ti polyhedra enter the TiC group, until all are directly related to at least one Ce octahedron as for $x = 0.30$.

Structural refinements (between 1 and 20 Å) were performed, refining cell parameters a and α, oxygen positions (constrained as above), Ti position (xxx) and isotropic displacement parameters for all atoms (there are 14 refinable free parameters, just three more than the simple model). In Table 2, the refined local cell parameters so obtained are reported. Even though the R_w local values are not significantly reduced in comparison with the simple model (see Fig. 8), the tilt model allows us to improve the 'goodness' of the analysis, providing results more consistent with observations than the simple model. Indeed, in comparison with a simpler rhombohedral starting model, a decrease in isotropic displacement parameter values (especially for oxygen atoms) and a substantial drop in related estimated standard deviation is obtained (Fig. 9 and Table S20 in the supporting information). The different size of the two B cations is then responsible for the local distortion, in particular regarding their different and

Figure 7
Simplified sketch which represents the refinement strategy (tilt model) applied for the oxygen positions for $x = 0.05$. Three oxygen groups are determined, depending on the cerium vicinity; the applied constraints determine different types of octahedra and allow their distortions and tilt.
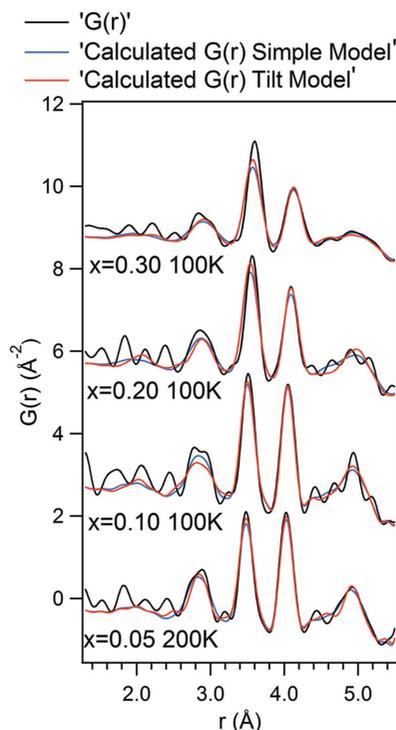

Figure 8
Comparison between fits obtained by the refinements of the simple model and tilt model.

distinct local oxygen environments. As reported in Fig. 10, titanium and cerium cations tend to induce different octahedral volumes, as the two cations locally maintain their own distances with O atoms (see supporting information for more details). The octahedral volumes tend to behave differently, as a function of temperature, depending on the amount of cerium in the corresponding sample. In samples with $x = 0.05$, $x = 0.10$ and $x = 0.20$, cerium-bearing and titanium-bearing octahedra have an approximately constant volume (around 13 Å^3 for the former and 11 Å^3 on average for the latter) as a function of temperature. Attention must be payed to the case of $x = 0.05$: Ti-bearing octahedra belonging to the TiC group (in red in Fig. 7) are too small and those belonging to the TiB group (in purple in Fig. 7) are too large with respect to the usual volume (10.7 Å^3) for TiO$_6$ octahedra (Kwei *et al.*, 1993). Note, however, that the two groups of octahedra are linked, sharing at least one oxygen atom, whose position within the unit cell is strongly correlated, in the refinement, with the other O-atom position (correlation value = −0.845). Despite various repetitions of the refinement, starting with slightly different oxygen positions to avoid any false-minimum situation, the results did not change. Nonetheless, if a weighted average is calculated, the average volume of TiC and TiB group octahedra is around 11 Å^3, similar to that of the other samples.

The most Ce-rich composition (BaTi$_{0.7}$Ce$_{0.3}$O$_3$) is the only one in which octahedral volumes change with temperature. Cerium- and titanium-bearing polyhedra have very different starting points at low temperature and tend to become more similar to each other with increasing temperature. However, each Ti-bearing octahedron is connected to at least one Ce-bearing octahedron (and may even be connected to five), making the Ti- and Ce-bearing polyhedral volumes highly correlated and inversely proportional. Any deduction based

on these volumes for the $x = 0.30$ sample must take this issue into account.

The results presented so far show a clear differentiation between Ce and Ti local oxygen environments. The two polyhedra maintain different volumes, as confirmed by Raman analysis (Canu *et al.*, 2018). Furthermore, as also observed in BZT (Laulhe *et al.*, 2009, 2010), the TiO$_6$ volumes are essentially constant, almost insensitive to the amount of doping, and approach values similar to those in pure BaTiO$_3$. On the other hand, the Ce octahedra are smaller than those of BaCeO$_3$ and have almost constant volume. The introduction of cerium into the structure produces a strain that is proportional to the amount of cerium in the samples (as shown in Fig. 2). Such strain, which is partly relieved by the creation of dislocations (see the TEM images in Fig. 4), affects the atomic structure *via* tilting and distortions of the polyhedra. As the difference in size of the two cations is very large, the strain induced as a consequence can also be capable of compressing the Ce−O
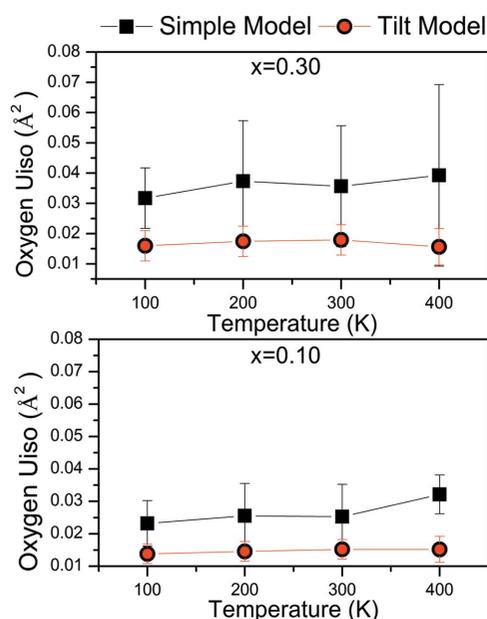

Figure 10
Volumes of octahedra, obtained by the tilt model in BaCe$_x$Ti$_{1-x}$O$_3$, compared as a function of temperature for different x values. Black circles refer to cerium-containing octahedra, while squares refer to the three titanium-bearing octahedra (their color depends on their distance from cerium-bearing octahedra): Ti octahedra near to those with cerium (TiC) are reported with red squares, those far from cerium (TiF) with blue squares and those between these two last groups (TiB) with purple squares. The volumes of the octahedra corresponding to the two end members at 300 K are also reported with two lines on the vertical axis: blue for BaTiO$_3$ (Kwei *et al.*, 1993) and black for BaCeO$_3$ (Knight, 2001).

Figure 9
Oxygen isotropic displacement parameters obtained by the refinements of the simple model and tilt model for compositions $x = 0.10$ and $x = 0.30$.
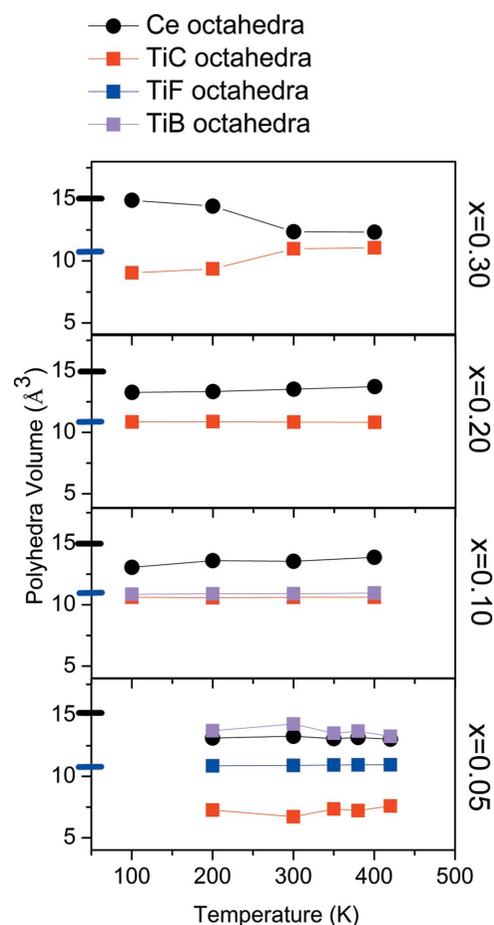
octahedra with respect to their sizes in unstrained pure $BaCeO_3$.

Moreover, the structural distortions found in the local structure are also likely to be involved in the polar behavior. Ferroelectric properties are related, as reported above, to the titanium displacement. Our results are shown in Fig. 11, where the displacements of titanium are calculated, along [111], from the center of the unit cell; in the figure, the local displacements (from the model refined above, in red in the figure) are compared with those found in the Rietveld refinements, where Ti and Ce were refined on the same site with fractional occupancies (average value, in black in the figure).

As a general result, the larger the local displacement, the smaller the Ce content. These large displacements in the low-cerium samples are related not to the volume of the octahedra (which is constant for all compositions) but instead to the distortion at the nearest-neighbor level. In other words, if the cerium concentration is large enough (as in $x = 0.20$ and $x = 0.30$), every single titanium atom is close to a large number of Ce-bearing octahedra and may be forced, by their presence, to

remain fixed or to move in a slightly different direction, yielding in both cases an average zero-displacement scenario. Conversely, in samples with a comparatively small amount of cerium, the number of Ce-bearing octahedra close to a Ti-bearing one is so low as to yield a large probability for a local correlation of titanium displacements along the cell body diagonal.

It is clear, then, that cerium introduction induces an increasing local distortion, which decreases the titanium local displacement correlation along [111] and thus the local spontaneous polarization. The local distortion, on the other hand, seems to influence, in a non-negligible way, the changes in the average structure. In fact, inspecting the α angle of the rhombohedral unit cell it is possible to envisage the deformation mechanism of the unit cell, with respect to the corresponding cubic cell. It is particularly interesting to compare it with the corresponding average value, *i.e.* the value coming from Rietveld refinement of the same data. The evolution of the α angle in the average and local structure is shown in Fig. 12. As a function of temperature, for each composition, the average α angle increases and achieves the ideal (cubic) value of 90° with different trends for the different compositions, *i.e.* the decreasing distortion with temperature is also
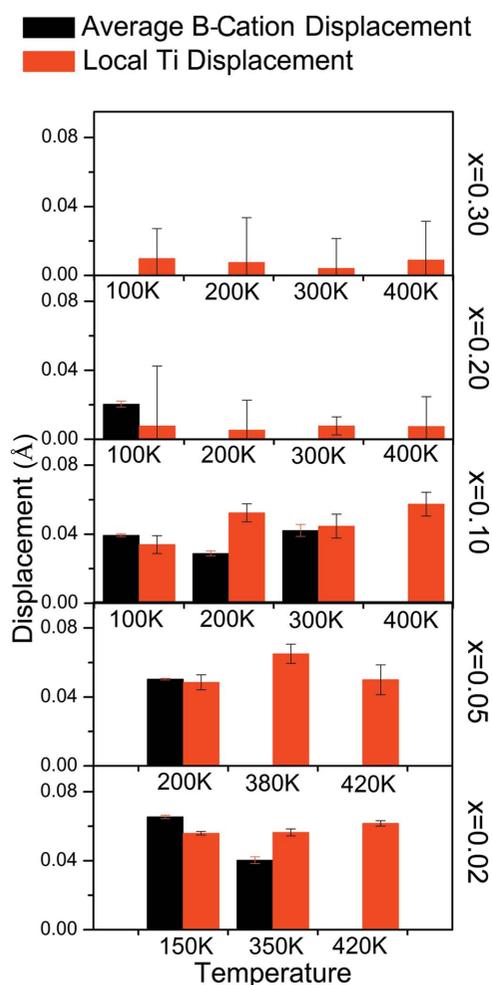

Figure 11
B-cation displacements, calculated from the center of cells, in the average and local structure are shown. In the local structure, the Ti displacement was obtained; in the average, titanium and cerium were constrained in the same position.
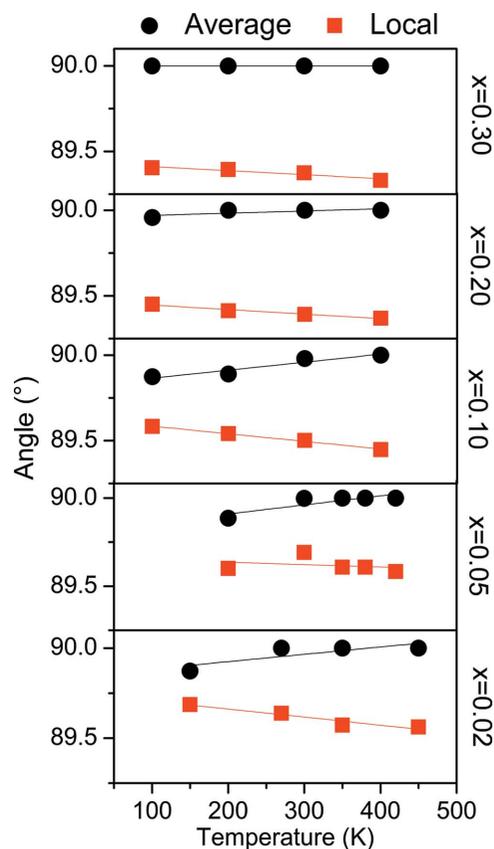

Figure 12
Average and local cell angle parameters. The average angle values for biphasic samples were reported for the predominant phase (Table 2). Local results for $x = 0.02$ were obtained by the simple model; for the others the tilt model was used. Calculated regression lines are shown as guides to the eye. Errors on single points are smaller than the symbol size.

influenced by the amount of cerium. If the cerium concentration increases, the distortions are smaller and the cubic phase occurs at lower temperatures (Fig. 12 and Table 2), decreasing the Curie temperature. At the local scale, the opposite occurs: the level of distortion increases (α departs from 90°) with increasing x and temperature: cerium introduction creates increasing disorder and distortion at the local level.

Therefore, the larger the local distortion, the lower the distortion in the average structure. This is a clear indication that cerium decreases the structural coherent correlation length and in turn the average correlation of the titanium displacements (Fig. 11). This interpretation is in good agreement with the modification of the polar behavior from conventional ferroelectric to relaxor (Canu et al., 2018).

The proposed local structural model, though not a unique solution to solve the observed disorder, has the essential benefit of (i) having few refinable parameters (just 14 versus 11 in the simple model) and (ii) being able to trace a new and clear link between the local structure and its effect on the average one, and on the evolution of the polar behavior.

4. Conclusions

The introduction of the large Ce cation into the $BaTiO_3$ structure induces variations in the phase transition sequence and modification of the average and local structure. The large difference in size between titanium and cerium generates strain, which is partly relieved through the creation of volume defects (dislocations) and which induces, at the atomic level, a severe structural distortion. The disorder increases with increasing cerium content at all temperatures.

(1) The local disorder is mainly related to the different behavior of the oxygen cage in Ce-bearing and Ti-bearing polyhedra, and can be ultimately be ascribed to the difference in size of Ce and Ti cations. The respective octahedra tend to preserve the volume of their corresponding end member's polyhedra (14.9 $Å^3$ for CeO_6 and 10.7 $Å^3$ for TiO_6), causing tilting and distortion of the oxygen cages.

(2) The local disorder has a great influence on the average structure and on the material properties. The local distortions increase with increasing cerium content, while the distortion of the average unit cell diminishes with a decrease of the Curie temperature.

(3) The local disorder model shows very small B-cation displacements for large cerium contents ($x = 0.20$ and $x = 0.30$, in particular), with consequent relaxor behavior. Cerium introduction, therefore, creates disorder that reduces the local structure coherent correlation length, thus limiting the average titanium displacement correlations and then the spontaneous polarization.

The structural model here refined showed how the modifications of the local structure and, in turn, of local polar order in Ce-substituted $BaTiO_3$ have a strong influence on macroscopic dielectric and ferroelectric properties.

5. Related literature

For further literature related to the supporting information, see Baur (1974) and Robinson et al. (1971).

References

Acosta, M., Novak, N., Rojas, V., Patel, S., Vaish, R., Koruza, J., Rossetti, G. A. & Rödel, J. (2017). Appl. Phys. Rev. **4**, 041305.

Ang, C., Yu, Z., Jing, Z., Guo, R., Bhalla, A. S. & Cross, L. E. (2002). Appl. Phys. Lett. **80**, 3424–3426.

Baur, W. H. (1974). Acta Cryst. B**30**, 1195–1215.

Billinge, S. J. L. & Thorpe, M. F. (1998). Editors. Local Structure from Diffraction. New York: Springer US.

Canu, G., Confalonieri, G., Deluca, M., Curecheriu, L., Buscaglia, M. T., Asandulesa, M., Horchidan, N., Dapiaggi, M., Mitoseriu, L. & Buscaglia, V. (2018). Acta Mater. **152**, 258–268.

Cohen, R. E. (1992). Nature, **358**, 136–138.

Comès, R., Lambert, M. & Guinier, A. (1970). Acta Cryst. A**26**, 244–254.

Confalonieri, G., Dapiaggi, M., Sommariva, M., Gateshki, M., Fitch, A. N. & Bernasconi, A. (2015). Powder Diffr. **30**, S65–S69.

Curecheriu, L. P., Ciomaga, C. E., Musteata, V., Canu, G., Buscaglia, V. & Mitoseriu, L. (2016). Ceram. Int. **42**, 11085–11092.

Curecheriu, L. P., Deluca, M., Mocanu, Z. V., Pop, M. V., Nica, V., Horchidan, N., Buscaglia, M. T., Buscaglia, V., van Bael, M., Hardy, A. & Mitoseriu, L. (2013). Phase Transitions, **86**, 703–714.

Egami, T. & Billinge, S. J. L. (2012). Underneath the Bragg Peaks: Structural Analysis of Complex Materials, 2nd ed., Pergamon Materials Series, Vol. 16. Oxford: Pergamon/Elsevier.

Farrow, C. L., Juhas, P., Liu, J. W., Bryndin, D., Bozin, E. S., Bloch, J., Proffen, T. & Billinge, S. J. L. (2007). J. Phys. Condens. Matter, **19**, 335219.

Fitch, A. N. (2004). J. Res. Natl Inst. Stand. Technol. **109**, 133–142.

Gatta, G. D., Merlini, M., Valdré, G., Liermann, H.-P., Nénert, G., Rothkirch, A., Kahlenberg, V. & Pavese, A. (2013). Phys. Chem. Miner. **40**, 145–156.

Glazer, A. M. (1972). Acta Cryst. B**28**, 3384–3392.

Ianculescu, A., Berger, D. C., Vasilescu, C. A., Olariu, M., Vasile, B. S., Curecheriu, L. P., Gajović, A. & Trușcă, R. (2016). Nanoscale Ferroelectrics and Multiferroics, edited by M. Algueró, J. M. Gregg & L. Mitoseriu. Chichester: John Wiley and Sons.

Jaffe, B., Cook, W. R. Jr & Jaffe, H. (1971). Piezoelectric Ceramics. London, New York: Academic Press.

Juhás, P., Davis, T., Farrow, C. L. & Billinge, S. J. L. (2013). J. Appl. Cryst. **46**, 560–566.

Juhás, P., Farrow, C., Yang, X., Knox, K. & Billinge, S. (2015). Acta Cryst. A**71**, 562–568.

Kishi, H., Mizuno, Y. & Chazono, H. (2003). Jpn. J. Appl. Phys. **42**, 1–15.

Knight, K. S. (2001). Solid State Ionics, **145**, 275–294.

Kwei, G. H., Lawson, A. C., Billinge, S. J. L. & Cheong, S. W. (1993). J. Phys. Chem. **97**, 2368–2377.

Laulhe, C., Hippert, F., Bellissent, R., Simon, A. & Cuello, G. J. (2009). Phys. Rev. B, **79**, 064104.

Laulhe, C., Pasturel, A., Hippert, F. & Kreisel, J. (2010). *Phys. Rev. B*, **82**, 132102.

Lei, C., Bokov, A. A. & Ye, Z. G. (2007). *J. Appl. Phys.* **101**, 084105.

Lu, D. Y., Han, D. D. & Sun, X. Y. (2012). *Jpn. J. Appl. Phys.* **51**, 071501.

Lutterotti, L., Matthies, S. & Wenk, H. (1999). *IUCr Commission on Powder Diffraction Newsletter*, **21**, 14–15.

Maiti, T., Guo, R. & Bhalla, A. S. (2008). *J. Am. Ceram. Soc.* **91**, 1769–1780.

Makovec, D., Samardžija, Z. & Kolar, D. (1996). *J. Solid State Chem.* **123**, 30–38.

Miura, K., Azuma, M. & Funakubo, H. (2011). *Materials*, **4**, 260–273.

Müller, K. & Berlinger, W. (1986). *Phys. Rev. B*, **34**, 6130–6136.

Müller, K., Berlinger, W., Blazey, K. & Albers, J. (1987). *Solid State Commun.* **61**, 21–25.

Park, Y. & Kim, Y. H. (1995). *J. Mater. Res.* **10**, 2770–2776.

Robinson, K., Gibbs, G. V. & Ribbe, P. H. (1971). *Science*, **172**, 567–570.

Shvartsman, V. V. & Lupascu, D. C. (2012). *J. Am. Ceram. Soc.* **95**, 1–26.

Souza, E. C. C. de & Muccillo, R. (2010). *Mater. Res.* **13**, 385–394.

Thomas, N. W. & Beitollahi, A. (1994). *Acta Cryst.* B**50**, 549–560.

Woodward, P. M. (1997). *Acta Cryst.* B**53**, 32–43.

Xiao, C. J., Jin, C. Q. & Wang, X. H. (2008). *Mater. Chem. Phys.* **111**, 209–212.

Yasmm, S., Choudhury, S., Hakim, M. A., Bhuiyan, A. H. & Rahman, M. J. (2011). *J. Mater. Sci. Technol.* **27**, 759–763.